A&A 378, 345–360 (2001)
DOI: 10.1051/0004-6361:20011240

Astronomy
&
Astrophysics

Kinematics of the local universe

IX. The Perseus-Pisces supercluster and the Tolman-Bondi model

M. O. Hanski[1], G. Theureau[2,3], T. Ekholm[4,1], and P. Teerikorpi[1]

[1] Tuorla Observatory, 21500 Piikkiö, Finland
[2] Observatoire de Meudon, 92195 Meudon Cedex, France
e-mail: `gilles.theureau@obspm.fr`
[3] Osservatorio di Capodimonte, Via Moiariello 16, 80131 Naples, Italy
[4] Observatoire de Lyon, 69561 Saint-Genis Laval Cedex, France

Received 24 June 1999 / Accepted 5 September 2001

Abstract. The matter distribution around the Perseus-Pisces (PP) supercluster is studied by comparing peculiar velocities given by the Kinematics of the local universe (KLUN) galaxy sample to those predicted by Tolman-Bondi (TB) models. To restrict the TB solutions we first solve the mass of the densest part of PP. This part is identified as a sphere at $(l, b) = (140.2°, -22.0°)$, $d \approx 50\,h^{-1}$ Mpc having a radius of $15\,h^{-1}$ Mpc. This sphere surrounds the main part of the PP ridge and four most prominent clusters of the region. Using virial-like mass estimators we calculate the cluster masses and obtain the upper and lower limits for the mass inside the $15\,h^{-1}$ Mpc sphere: $M_{\rm PP} = 4$–$7\,h^{-1}\,10^{15} M_{\odot}$. This corresponds to a mass overdensity $\delta_{\rm PP} \approx 4$, or $\rho_{\rm PP} = 1 - 2\,\rho_{\rm cr}$. Mass to light ratios of the clusters are $M/L = 200 - 600\ h\,M_{\odot}/L_{\odot}$, giving mass density ratio $\Omega_0 = 0.1 - 0.3$, if the value of M/L is assumed to be representative elsewhere in the universe. We estimate a radial density distribution around the PP core using two toy models and a smoothed density distribution observed for IRAS galaxies. The cosmological density parameters $(\Omega_0, \Omega_\Lambda)$ and the PP mass are free parameters in the TB calculations. The KLUN velocities, obtained by Tully-Fisher relation and the normalized distance method, are adjusted by the Local Group (LG) infall velocity towards PP. Comparison of the TB velocities to KLUN data points indicates that the infall velocity $v_{\rm inf} < 100$ km s^{-1}. Allowing $M_{\rm PP}$ to vary within the limits given above we get constraints for the value of Ω_0; $\Omega_0 = 0.2$–0.4 are prefered to the more extreme values, $\Omega_0 = 0.1$ or 1. A choice of either $\Omega_\Lambda = 1 - \Omega_0$ or 0 do not cause any significant changes in the results. The validity of the TB model in complex environments is studied with an N-body simulation. There we see that the radially averaged velocity fields around simulated clusters are compatible with the corresponding TB velocities. This confirms the applicability of the TB model around large galaxy concentrations, providing that smoothed density and radially averaged velocity fields are used.

Key words. galaxies: clusters: general – galaxies: clusters: Pers-Pisc supercluster – cosmology: theory – large-scale structure of the universe

1. Introduction

Tolman-Bondi (TB) model is the analytical solution of a spherically symmetric mass distribution in an expanding universe (Tolman 1934; Bondi 1947). It has been succesfully applied to the Virgo system by Teerikorpi et al. (1992) and, recently, by Ekholm et al. (1999) for describing the peculiar velocity field and estimating the total mass of the system, even though the galaxy distribution in Virgo deviates notably from spherical. Motivation for the use of the TB model is that it is *simple* and *analytical*. It is a first step towards approximating an inhomogeneous universe. Bondi (1947) himself wrote that "the assumption of spherical symmetry supplies us with a model which lies between the completely homogeneous models of cosmology and the actual universe with its irregularities".

TB results are valid with appropriate smoothing; the observed velocity field must be averaged over concentric shells around a galaxy concentration, when compared to the TB results. Thus the TB model does not give the results in as much details as the various more commonly used gravitational instability – reconstruction methods. On the other hand, it does not require any assumptions for the breakdown of the theory in the non-linear region.

In order to test whether the TB model may be applied to an apparently still less favourable situation than Virgo, we study the Perseus-Pisces supercluster, where a TB-like deviation in the Hubble flow has already been observed

---

Send offprint requests to: M. Hanski,
e-mail: `mihanski@astro.utu.fi`

(Theureau et al. 1998a). Our criterion for the success of the TB method is whether the mass inferred using TB is comparable to virial and luminosity × M/L estimate for the region, and whether the peculiar velocity field is adequately described by the model.

The local $d < 70\ h^{-1}$ Mpc[1] universe is dominated by two large mass concentrations, the Great Attractor and the Perseus-Pisces (PP) complexes. According to Sigad et al. (1998) and Dekel et al. (1999) both regions have overdensities $\delta = 1$–1.5, where $\delta \equiv [\rho(x) - \bar{\rho}]/\bar{\rho}$, $\rho(x)$ is the local, and $\bar{\rho}$ the average density. Both studies used a Gaussian smoothing of $12\ h^{-1}$ Mpc and assumed $\Omega_0 = 1$. Thus the velocity field surrounding PP should reveal a strong infall towards the supercluster's center of mass. For a galaxy at around half way from PP to us the infall velocity should be $\approx$500 km s^{-1}. However, the infall signature is difficult to reveal because of large uncertainties in redshift independent distance measurements, e.g. those provided by Tully-Fisher (TF) or Fundamental Plane (FP) methods. Uncertainties are caused by statistical biases difficult to correct for in a heterogeneous environment. Additional inaccuracies are raised by the filamentary shape of the structure, consisting of an alignment of several subclusters, which complicates considerably any attempt to model the velocity field.

1.1. Previous studies of Perseus-Pisces

In the past ten years PP has been investigated by numerous authors using various distance criteria and statistical methods. The region is now well covered by great amount of data. From a large reshift sample of 3311 galaxies in the region bounded by $22^{\rm h} <$ RA $< 4^{\rm h}$, $+20° <$ Dec. $< +50°$, Wegner et al. (1993) described the Perseus-Pisces complex as follows: the supercluster consists of a continuous arrangement of high density clusters and groups, among which the Pisces, A262, and Perseus (A426) clusters are the most prominent features. Its main ridge extends at least $50\ h^{-1}$ Mpc from Pegasus eastward to the Perseus cluster, with a width in the plane of the sky of about 5–10 h^{-1} Mpc, and a typical depth in redshift of 250–500 km s^{-1}. All the objects in the ridge are lying roughly at the same distance from us, at $\sim$5000 km s^{-1}.

First kinematical studies (Willick 1990, 1991; Courteau et al. 1993) based on an r-band TF sample of 355 galaxies, suggested that the whole structure takes part on a large scale flow defined by the Great Attractor (see e.g. Lynden-Bell et al. 1988; Dekel 1994), with a mean velocity of $\sim$350 km s^{-1} towards the Local Group (LG). Han & Mould (1992) confirmed this result independently using a whole sky TF sample of 21 clusters. Hudson et al. (1997) combined their inverse FP relation measurements of seven clusters in the PP region with data of nine other clusters from the literature and concluded that the whole region has a mean CMB frame bulk motion of 420 ± 280 km s^{-1} towards galactic coordinates $(l, b) = (262°, -25°)$. POTENT reconstruction method of the density and velocity field for Mark III galaxies (Dekel et al. 1999) gave different results. There it was found that the center of PP is roughly at rest in the LG frame and the regions between the LG and PP are infalling towards PP.

Most studies of the velocity field of galaxies suggest that the kinematics of the local universe can be described by a model in which galaxies are infalling to two mass concentrations, one in PP and one in Hydra-Centaurus (e.g. Han & Mould 1992; Dekel et al. 1999). However, Freudling et al. (1995) and da Costa et al. (1996) used a method of analysis, based on Monte-Carlo simulations, in order to control biases and gain a better sampling of the sky. Their studies revealed a clear infall motion towards PP, while the GA was found less dominant than originally believed.

The differences in the results stated above may be caused by uncertainties in the reconstruction method, in the corrections for the selection effects, and/or in the distance indicator calibration. For example, an error in the TF zero point would cause a systematic error that resembles a Hubble flow in the peculiar velocity field. Dekel et al. (1999) also note that the results in the PP region are more sensitive to noise than the other regions.

1.2. What is new in our approach to PP?

In a previous study using the KLUN galaxies, a full infall pattern, both in the front and the backside of the PP supercluster was shown, for the first time. A new Malmquist bias correction method for the TF distance data was used (Theureau et al. 1998a). In the present paper we investigate the dynamics of galaxies in the PP surroundings in more detail. We study the spatial distribution and peculiar velocities of the galaxies using the Malmquist corrected TF distances. The observed velocity field is averaged over spherical shells around the PP center and compared to the results given by TB calculations.

The outline of the paper is as follows: in Sect. 2 we briefly present the data and summarize the normalized distance method (NDM) that has been used for deriving unbiased average distances and peculiar velocities. In Sect. 3 we calculate the virial masses of the most prominent clusters in the PP region and estimate the mass of the whole central region of PP from these masses. Section 4 includes a description of the Tolman-Bondi model and its application to PP. The model is also tested on an N-body simulation of galaxy clusters (Sect. 4.2). In Sect. 5 we compare the TB model to the infall pattern observed with the KLUN data. Finally, the main results are summarized in Sect. 6.

2. Towards unbiased peculiar velocities

The following notation is appointed for different distance and velocity variables:

- d for distances from the LG;

---

[1] $h = H_0/(100$ km s^{-1} Mpc$^{-1})$.

- r for distances from the PP center;
- capital R for fixed distances: $R_{\rm PP}(= 50\ h^{-1}$ Mpc) is the distance between the LG and the PP center, $R_{\rm s}(= 15\ h^{-1}$ Mpc) is the radius of the main region of the PP concentration;
- small v for peculiar velocities, $v_{\rm r}$ is the peculiar velocity with respect to the PP center, $v_{\rm d}$ is the peculiar velocity with respect to the LG;
- capital V for observed (Hubble flow + peculiar) velocities, corrected for the infall towards Virgo as described in Sect. 2.1.

Exceptions are

- quantities with subindex 25: D_{25} is the standard notation for the isophotal $B = 25$ mag diameter of a galaxy and R_{25} is the corresponding axis ratio;
- $V_{\rm m}$ is the maximum of the rotational velocity of a galaxy.

For the Hubble constant we assume $H_0 = 60$ km s^{-1} Mpc^{-1}, or indicate it by the term $h \equiv H_0/(100$ km s^{-1} Mpc$^{-1})$. The value is needed in calculating the radial part of the peculiar velocities,

$$v_{d,{\rm obs}} = V - H_0 d, \qquad (1)$$

where the subscript "obs" emphasizes that only this component of the peculiar velocity can be directly observed.

The main difficulties in velocity field studies are caused by the large uncertainties in distance determination and by the resulting biases. Attempts to overcome these problems require a few things. Firstly, one must know thoroughly the sample, how it was collected, and to which extent it can be assumed complete. Secondly, systematic effects in the distance criterion have to be modeled, so that one can derive for a given application an unbiased set of distances. In particular, biases will be different if one estimates peculiar velocities at a given derived distance, at a given true distance, or at a given observed radial velocity. Thirdly, the sample has to be deep enough and should cover a sufficiently large solid angle in the sky for the average relations, needed for the bias correction, to be free from local perturbations in the density or the velocity field. This last requirement is similar as needed for a satisfactory determination of the Hubble constant.

2.1. The data

We use the KLUN (Kinematics of the local universe) sample consisting of 6600 spiral galaxies having measurements of isophotal diameter D_{25}, HI line width, radial velocity, and B-magnitude. This sample has been fully described in previous papers of this series, e.g. by Theureau et al. (1997), so we only summarize here the main characteristics.

KLUN is selected according to apparent diameter, and is complete down to $D_{25} = 1\farcm6$ (Paturel et al. 1994), covering the type range Sa–Sdm (T = 1–8). The data are extracted from LEDA (Lyon-Meudon Extragalactic Database, Paturel et al. 1997) and complemented with optical redshifts measured with ESO and OHP telescopes, and HI spectra obtained with Nançay and Parkes radio telescopes (Bottinelli et al. 1992, 1993; di Nella et al. 1996; Theureau et al. 1998b). According to LEDA precepts, all astrophysical parameters have been homogenized and reduced to a standard and common system (Paturel et al. 1997). Isophotal D_{25} diameters and apparent B-magnitudes are corrected for galactic extinction according to Fouqué & Paturel (1985), and for inclination, i.e. the opacity effect, as explained in Bottinelli et al. (1995). HI line widths, reduced to the standard levels of 20% and 50%, are corrected for internal velocity dispersion according to Tully & Fouqué (1985). Heliocentric radial velocities are changed to the rest frame of the LG centroid following Yahil et al. (1977) and corrected for a Virgocentric component, assuming an infall of the LG towards the Virgo cluster $v_0 = 200$ km s^{-1} (Theureau et al. 1997; Jerjen & Tammann 1993) and a radial velocity of Virgo $V_{0,{\rm Vir}} = 980$ km s^{-1} (Mould et al. 1980), within a linear infall model (Peebles 1976).

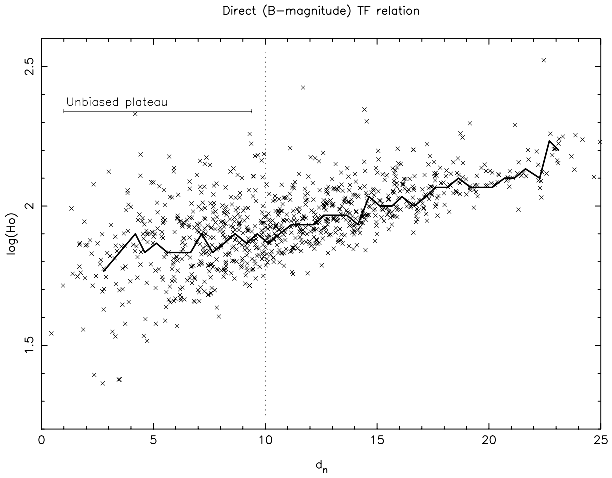

Fig. 1. The $\log H_0$ vs. $d_{\rm n}$ diagram of KLUN galaxies. The line, indicating the average $\langle \log H_0\rangle(d_{\rm n})$, is (approximately) horizontal in the unbiased region at small $d_{\rm n}$. Malmquist bias makes the curve to rise at larger $d_{\rm n}$.

In the TF relation studies we need to make some restrictions to the data. Galaxies close to the Galactic plane ($|b| \leq 15°$) are excluded due to the large uncertainties in the Galactic extinction correction. Face-on galaxies, $\log R_{25} < 0.07$, are excluded to prevent large errors on calculation of the rotational velocity parameter $p \equiv \log V_{\rm m}$, where $V_{\rm m}$ is the maximal rotational velocity of a galaxy, measured from the HI line width.

Absolute TF distances are obtained using the calibration given by Theureau (1998). TF scatter was there reduced by 30% by taking into account the dependence of the TF zero point on mean surface brightnesses of the galaxies. The NDM first order Malmquist corrections are calculated on the basis of the whole sky sample, according to Theureau et al. (1998a). The sample with thus corrected TF distances, restricted to the strictly diameter complete part, contains finally 2800 spiral galaxies.

2.2. The normalized distance method (NDM)

The concept of normalized distances was introduced in a theoretical discussion by Teerikorpi (1984). The method was first applied by Bottinelli et al. (1986) and improved in a series of papers, most recently by Theureau et al. (1997). A theoretical description in terms of probability densities was given by Theureau et al. (1998a), where the authors showed that the method can be extended to make Malmquist bias corrections to galaxy distances even beyond the so-called unbiased plateau. The unbiased plateau has been profitably used for determination of the unbiased value of H_0 and has the advantage that one does not need model-dependent bias corrections.

In order to understand how the NDM works, let us define classes of galaxies as follows: objects belong to a given class if they have identical values of log rotational velocity p, Galactic extinction correction $a_{\rm g}$, inclination R_{25}, morphological type T and mean surface brightness Σ. The main idea of the NDM is that for a given magnitude or diameter limited sample, and for a given TF scatter the behaviour of the Malmquist bias[2] as a function of true distance is similar for all galaxies belonging to the same class. The class is assumed to have a Gaussian distribution of absolute magnitudes. Then, for each class, there is a unique curve of evolution of the bias, which is conveniently expressed as the curve of observed average value of the Hubble parameter $\langle\log H_0\rangle = \langle\log V_{\rm c} - \log d_{\rm TF}\rangle$ vs. distance (d), where $d_{\rm TF}$ is the distance given by TF relation,

$$\log d_{\rm TF} = a_{\rm TF}p + b_{\rm TF}(\Sigma) - \log D_{25} - \log\frac{\pi}{108}; \qquad (2)$$

$a_{\rm TF}$ is the TF slope, $b_{\rm TF}(\Sigma)$ the TF zero point, dependent on the surface brightness Σ of the galaxy, and $\frac{\pi}{108}$ is a constant for converting the units (linear TF-diameter in kpc and D_{25} in $0\farcm1$ to $d_{\rm TF}$ in Mpc).

Essentially, the normalized distance technique means superimposing all the bias curves $\langle\log H_0\rangle(d)$ of the different classes of objects by using an appropriate scaling on the distance:

$$d_{\rm n} = d\cdot f(p, a_{\rm g}, R_{25}, T, \Sigma). \qquad (3)$$

As a result, the amplitude of the bias can be expressed merely as a function of the normalized distance ($d_{\rm n}$), the apparent limit of the sample ($m_{\rm lim}$ or $D_{25,\rm lim}$), and the TF scatter ($\sigma_{\rm TF}$). Figure 1 shows the $\langle\log H_0\rangle$ vs. $d_{\rm n}$ diagram of KLUN galaxies in the case of the B magnitude TF relation. The unbiased part of the sample is identified as a plateau of $\langle\log H_0\rangle$ = constantat, at low values of $d_{\rm n}$. Note, however, that for calculation of $d_{\rm n}$, one needs the true distance d, usually derived as the so-called kinematical distance, e.g. in the case of the Hubble law $d = d_{\rm kin} \equiv V/H_0$.

The average bias correction is valid only if the following assumptions are fulfilled:

- *H1*: the sample is complete and strictly diameter (magnitude) limited;
- *H2*: TF residuals follow a Gaussian distribution, and the TF scatter does not depend on the value of p;
- *H3*: the selection in apparent diameter (magnitude) is independent of the selections in redshift and p;
- *H4*: the radial velocity field integrated over all the directions vanishes, i.e. except the Hubble flow, there is no coherent flow at the scale of the whole sample.

Assumption *H1* is obtained by applying a strict cut-off at the completeness limit of the sample. *H2* is in agreement with what is observed in the case of the B-band TF relation (Theureau et al. 1997). *H3* might be difficult to prove, if observational errors on apparent magnitudes or diameters are correlated with the errors on p: both are linked to the inclination of the galaxy through the internal extinction correction and the de-projection of the observed HI line width. However, this effect is insignificant in the case of the diameter TF relation.

As for assumption *H4*, a list of recent measurements of large-scale bulk motions is given by Strauss (2000). The list is somewhat divergent; roughly half of the surveys find no bulk flow at scales $V \geq 6000$ km s^{-1}, the rest claim bulk flows of 300–600 km s^{-1}. We will return to the question of large-scale flow within the KLUN sample in the future, for now we assume that assumption *H4* is true for our data.

Finally, the corrected distance is given by

$$\log d_{\rm c} = \log d_{\rm TF} + \sqrt{\frac{2}{\pi}}\cdot\frac{\sigma_{\rm TF}\exp\left(-\frac{(\omega-\log D_{25,\rm lim})^2}{2\sigma_{\rm TF}^2}\right)}{1-{\rm erf}\left(\frac{\omega-\log D_{25,\rm lim}}{\sqrt{2}\sigma_{\rm TF}}\right)}, \qquad (4)$$

(Theureau et al. 1998a), where the (log) normalized distance is marked with ω,

$$\omega \equiv \log d_{\rm n} = \log d + a_{\rm TF}(2.7-p) + 0.094a_{\rm g} - C\log R_{25} - b_{\rm TF}(\Sigma).$$

Here $d = V/H_0$ and parameter C defines the correction for inclination (Bottinelli et al. 1995). For a single galaxy class and usual kinematical distance, an analogous formula was derived by Teerikorpi (1975). It has also appeared in the "triple-value correction method" of Sandage (1994).

We emphasize that this correction is statistical in nature. When applied to an individual galaxy, it gives an accurate *average* correction only if the velocity field model (providing $d_{\rm kin}$ and d) is correct. When the velocity field is distorted, say, in the direction of a supercluster, it still gives a first order correction, but a complete correction would require an iterative procedure (see Sect. 5.3). Even the first order correction essentially improves the derived velocity field, as was shown by Theureau et al. (1998a) for the PP supercluster, but it is notable that the peculiar velocities will be somewhat suppressed if only a first order correction is done.

---

[2] In fact the Malmquist bias of the 2nd kind, as termed by Teerikorpi (1997).

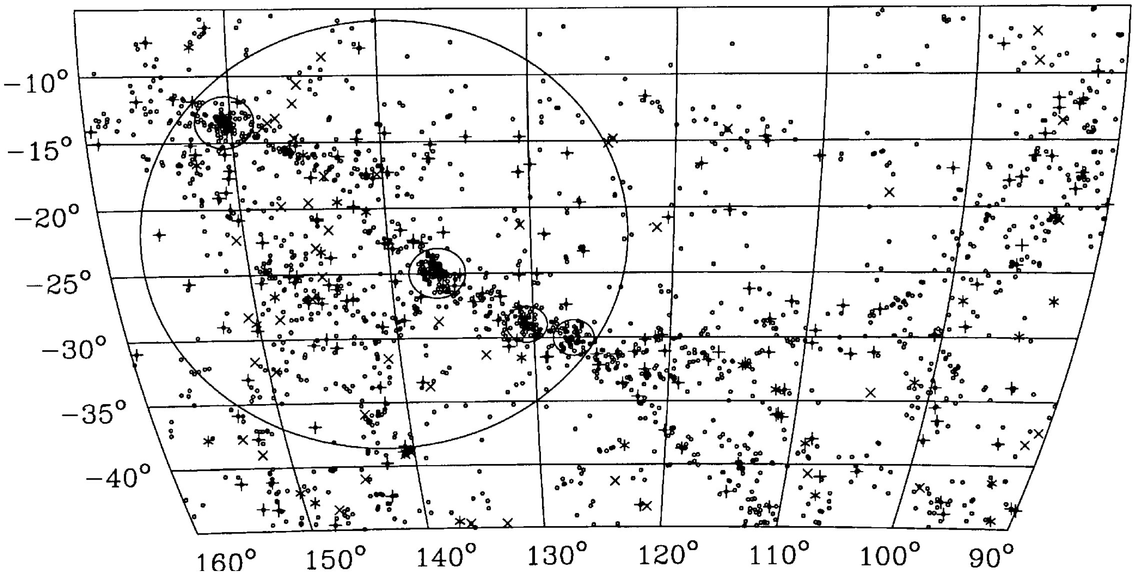

Fig. 2. LEDA (o) and KLUN galaxies (+, ∗ and ×) in the PP region. Large circle is the 15 h^{-1} Mpc sphere at (140.2°, −22.0°) containing the main concentration. Small circles are the four densest clusters, Perseus, A262, 0122+3305 and Pisces, from up left to down right.

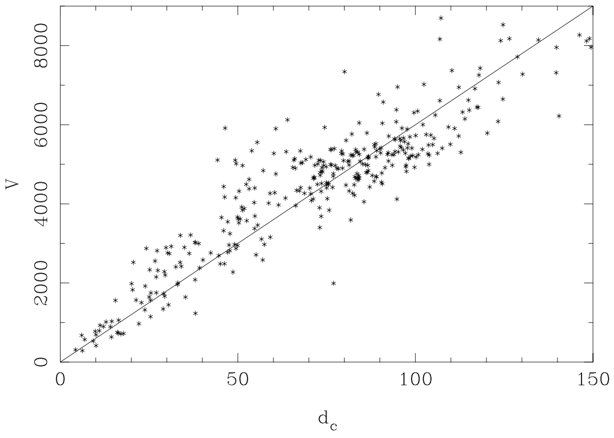

Fig. 3. The Hubble diagram of KLUN galaxies in the PP region. d_c is the NDM corrected TF distance.

3. The virial mass of Perseus-Pisces

Figure 2 shows a map of the PP region. Circles stand for galaxies from LEDA, having radial velocities between 3000 and 7000 km s^{-1}. This limitation allows us to look at the main part of the PP concentration, lying at $V \approx 5000$ km s^{-1}, practically free from any contamination from fore/background objects. LEDA is regularly updated for all published data and thus contains all the recent PP-surveys.

Symbols other than circles are KLUN galaxies. +:s are objects within the velocity interval stated above, ∗:s have $V > 7000$ km s^{-1} and ×:s $V < 3000$ km s^{-1}. Only the KLUN galaxies satisfying the completeness limit, $D_{25} > 1.'6$, and other criteria demanded by our TF-method (see Sect. 2.2), are plotted. In total, Fig. 2 contains 2016 LEDA galaxies and 266 objects from KLUN.

Table 1. Galactic coordinates, numbers of galaxies, mean velocities, virial radii in degrees and in h^{-1} Mpc, upper and lower estimates of masses in $h^{-1}10^{14}M_\odot$, and mass to light ratios in $hM_\odot/L_\odot$, of the four largest PP clusters in radial velocity interval 3000–7000 km s^{-1}. Clusters are 1) Perseus, 2) A262, 3) 0122+3305, and 4) Pisces.

	l	b	N	V	θ_v	r_v	M	M/L
1	150.5	−13.5	152	5144	2.0	1.8	8–12	310–490
2	136.7	−25.0	104	4878	2.0	1.7	4–6	210–370
3	130.5	−29.0	67	5085	1.5	1.3	4–6	260–510
4	127.1	−30.0	63	5096	1.5	1.3	3–5	270–550

In Fig. 3 the Hubble diagram of the KLUN PP region galaxies is shown. The line corresponds to the Hubble law with $H_0 = 60$ km s^{-1} Mpc^{-1}. The infall towards PP is seen as the surplus of galaxies above the Hubble line at small distances and below the line at large distances.

We seek a rough estimate for the amount of matter in the PP region. First we determine the masses of the densest clusters in the region. We define the densest consentrations as the ones having the projected galaxy overdensity $\delta_{2\mathrm{D}} > 10$. Here $\delta_{2\mathrm{D}}(x) = (\rho_{2\mathrm{D}}(x) - \bar{\rho}_{2\mathrm{D}})/\bar{\rho}_{2\mathrm{D}}$, the two dimensional sky densities $\rho_{2\mathrm{D}}(x)$ are calculated in 1 degree^2 regions, and $\bar{\rho}_{2\mathrm{D}}$ is the mean value of the whole region shown in Fig. 2. The limiting factor 10 has no special physical meaning. It was chosen to give a reasonable number of dense galaxy concentrations. There are four clusters satisfying this criterium. The characteristics of these clusters are listed in Table 1. Masses are estimated using the virial theorem and the alternative methods presented by Heisler et al. (1985), see Table 2 below. The effects of possible outsiders and interlopers are tested by using various radii and redshift intervals in defining cluster members. Table 2 shows some of the results. For the

Table 2. Virial, projected, median and average masses by methods of Heisler et al. (1985), and the corresponding M/L ratios of the four PP clusters. Different radii θ_v are used for each. The figures indicate that virial and median mass estimators seem to be less affected by outsiders ($\mathrm{d}M/\mathrm{d}\theta_\mathrm{v}$ small) than projected and average masses. Projected mass is also very sensitive on the coordinates chosen for the cluster center. This table is calculated for galaxies having 3000 km s^{-1} $< V <$ 7000 km s^{-1}. Changing the V interval affected all the mass estimators similarly. The limits for V and the cluster virial radii are chosen partly by eye, simply by using limitations defining a compact galaxy concentration, and partly by requiring certain level of stability for the obtained values of mass. The values adopted in Table 1 are the lowest and the highest values from the rows $\theta_\mathrm{v} = 2.0°$ for Perseus and A262, and $\theta_\mathrm{v} = 1.5°$ for 0122+3305 and Pisces. Units: $[M] = h^{-1}10^{14}M_\odot$, $[M/L] = hM_\odot/L_\odot$.

θ_v	N	$\langle V\rangle$	M_vi	M_pr	M_me	M_av	M/L
Perseus							
1.0°	115	5107	5.5	6.6	4.9	5.5	244–362
1.5°	131	5131	6.4	7.9	6.1	6.9	275–393
2.0°	152	5144	8.1	11.8	8.1	10.1	309–493
2.5°	172	5119	9.4	14.3	10.0	12.5	314–525
3.0°	183	5148	10.3	16.1	11.2	14.2	320–546
A262							
1.0°	62	4965	2.8	3.4	2.3	2.7	195–342
1.5°	93	4915	3.6	4.1	2.9	3.5	168–284
2.0°	104	4878	4.3	5.6	3.8	4.6	206–369
2.5°	116	4892	5.1	7.0	4.7	5.6	220–405
3.0°	132	4924	5.9	8.1	5.6	6.6	233–410
0122+3305							
1.0°	49	5036	2.7	2.9	2.5	2.5	236–333
1.5°	67	5085	4.5	5.9	3.6	4.7	260–511
2.0°	88	5063	5.6	7.1	4.5	5.8	261–502
2.5°	98	5037	6.2	7.9	5.1	6.5	266–499
3.0°	125	5052	7.1	9.1	5.5	7.5	220–440
Pisces							
1.0°	47	5073	1.9	2.9	1.7	2.1	203–409
1.5°	63	5096	2.9	4.6	2.7	3.3	270–550
2.0°	77	5105	4.2	7.1	3.7	5.1	308–713
2.5°	95	5107	5.2	8.3	4.7	6.1	329–702
3.0°	122	5187	9.0	16.2	7.1	11.6	385–1074

mass evaluations in Table 1 we adopt V-interval of 3000–7000 km s^{-1}, and use virial radii of 2° for Perseus and A262, and 1.5° for 0122+3305 and Pisces. These radii are drawn in Fig. 2.

For the M/L ratio derivations in Tables 1 and 2 we calculate the total luminosities of the clusters from LEDA B-band brightnesses and estimate selection effects using the Schechter function

$$\phi(\mathcal{M}) \propto 10^{0.4(\mathcal{M}^*-\mathcal{M})(\alpha+1)} \exp\left[-10^{0.4(\mathcal{M}^*-\mathcal{M})}\right], \qquad (5)$$

expressed here in terms of absolute magnitude $\mathcal{M}$. The characteristic magnitude, $\mathcal{M}^*$, and slope, α, of the function are found by fitting Eq. (5) to the observed magnitude distribution. Since the Perseus cluster shows clearly different features from the other three clusters, the fitting for it is done separately. Obtained parameters are $\alpha = -1.46^{+0.22}_{-0.26}$ and $\mathcal{M}^* - 5\log h = -19.6^{+0.4}_{-0.3}$ for Perseus, and $\alpha = -1.51^{+0.37}_{-0.23}$ and $\mathcal{M}^* - 5\log h = -20.4^{+0.7}_{-0.7}$ for the others (Fig. 4). The errors are bootstrap $1\,\sigma$ confidence limits.

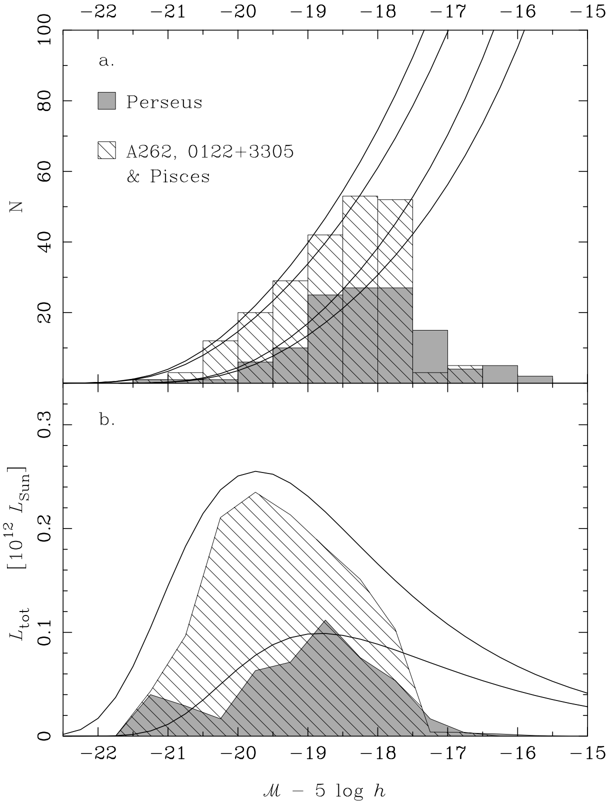

Fig. 4. a) shows the observed absolute magnitude histograms for the Perseus galaxies (gray bins) and the three other clusters combined (hatched bins). Two Schechter function curves are drawn on both of these histograms. Lower lines are fitted to the histograms at $\mathcal{M} - 5\log h < -18$, upper lines are calculated by assuming completeness of 80% for Perseus and 85% for the other clusters, following the latitude dependent completeness estimate by Marinoni et al. (1999). **b)** shows the corresponding total luminosities in 0.5 magnitude bins. The lines are the values predicted by the upper Schechter curves of **a)** By estimating the ratio of the gray/hatched areas to total areas under the Schechter curves in **b)** we can calculate the amount of luminosity of non-detected galaxies. This is $42^{+3}_{-2}\%$ for Perseus and $40^{+8}_{-3}\%$ of the total luminosity for the others.

Marinoni et al. (1999) observed for galaxies in large groups $\alpha = -1.28\pm0.18$ and $\mathcal{M}^* - 5\log h = -20.38\pm0.31$. The difference between our value for Perseus $\mathcal{M}^*$ and the one given by Marinoni et al. is probably due to environmental differences between Perseus and other clusters and/or uncertainties in the brightness measurements caused by the Galactic absorption. Comparison of the total observed luminosities of the clusters to the values obtained by integrating Eq. (5) indicates that the contribution of non-detected galaxies is $\mathcal{P}_\mathrm{nd} = 42^{+3}_{-2}\%$ for Perseus and $\mathcal{P}_\mathrm{nd} = 40^{+8}_{-3}\%$ for the others, with $1\,\sigma$ bootstrap errors. The limits for the M/L ratios are then calculated with the upper and lower mass values from Table 1 and by estimating the true total luminosities to be $1/(1-\mathcal{P}_{\rm nd})$, i.e. 1.64–1.80 (Perseus) and 1.60–1.95 (others) × the observed values. Resulting M/L ratios are all in the range of 210–550 $h\ M_\odot/L_\odot$, in good agreement with other recent estimations of M/L ratios of rich clusters (e.g. Bahcall et al. 1995; Carlberg et al. 1997).

Adding up the masses of the four clusters in Table 1, we get $\sim$ 2–3 $h^{-1}\ 10^{15} M_\odot$. The center of mass of PP, using these clusters, is at $V_{\rm C} = 4965$ km s^{-1}, $(l_{\rm C}, b_{\rm C}) = (140.2°, -22.0°)$. Distances of the clusters from this point are 11.5, 3.9, 9.9 and 12.5 h^{-1} Mpc. A sphere at $(l_{\rm C}, b_{\rm C})$, with a radius of 15 h^{-1} Mpc surrounds all these main concentrations. In addition to the four clusters, this sphere contains 513 other galaxies. If we assume that the M/L ratio does not grow in scales larger than the rich clusters, as suggested by Bahcall et al. (1995, 2000), we can then estimate $M_{\rm PP} \approx$ 4–7 $h^{-1}\ 10^{15} M_\odot$, where $M_{\rm PP}$ is the mass inside the 15 h^{-1} Mpc sphere. The selection effects are assumed to be the same for the galaxies in the four clusters and for the other galaxies in the 15 h^{-1} Mpc sphere.

However, there is some evidence that M/L increases on scales larger than clusters. For example Small et al. (1998) found the mass to light ratio to be 564 $h\,M_\odot/L_\odot$ for the Corona Borealis supercluster and 726 $h\,M_\odot/L_\odot$ for a background supercluster. Small et al. used the virial and projected mass estimators for the whole bound supercluster. The Tolman-Bondi calculations (next section) show that the PP is also bound, so we may apply the virial estimators on the PP also. We get $M_{\rm PP} = 2.6$, 4.2, 2.8, and 3.3 $h^{-1}\ 10^{15}\ M_\odot$ for the 836 galaxies in the central 15 h^{-1} Mpc sphere in PP, using the virial, projected, medium, and average mass estimators, respectively. The corresponding sum of the galaxy luminosities gives 4.4 $h^{-2}\ 10^{12}\ L_\odot$. Taking from above the more conservative limits for the number of non-detected galaxies, this number is then increased by a factor 1.60–1.95, giving the total luminosity $L_{\rm PP}$ = 7.0–8.5 $h^{-2}\ 10^{12}\ L_\odot$. Finally, the mass to light ratio, using these values, is 330–600 $h\,M_\odot/L_\odot$. However, since this mass for the whole PP core is about equal to the sum of the four clusters derived above, we doubt the accuracy of the virial and other estimators in this case, and adopt the values 4–7 $h^{-1}\ 10^{15}\ M_\odot$ for $M_{\rm PP}$.

These upper and lower limits for $M_{\rm PP}$ give a mean density $\rho_{\rm PP} \approx$ 2–4 $h^2\ 10^{-26}$ kg m$^{-3} \approx$ 1–2 $\rho_{\rm cr}$, where $\rho_{\rm cr}$ is the critical density of the universe. In terms of mass overdensity this is $\delta_{\rm PP} \approx 4$, assuming $\Omega_0 \approx$ 0.2–0.4. The lower value of Ω_0 here corresponds naturally to the lower limit of $\rho_{\rm PP}$, and high Ω_0 to the higher $\rho_{\rm PP}$. The result is in agreement with the value $\delta \approx 1$ ($\Omega_0 = 1$) by Sigad et al. (1998) and Dekel et al. (1999).

4. Tolman-Bondi method

4.1. Theoretical background

Tolman-Bondi (TB) equations determine the kinematics of a spherically symmetric mass concentration in an expanding universe (see e.g. Olson & Silk 1979; Ekholm 1996 for main features of TB, and Teerikorpi et al. 1992; Ekholm & Teerikorpi 1994; Ekholm et al. 1999, 2000 for some recent applications). In practice we study the behaviour of a spherical layer of matter at distance r from the center of symmetry. Each of these shells have two dynamical constants. In Newtonian terms we can think of these constants as the mass inside the radius of the shell,

$$M(r) = \int_0^r 4\pi\rho(r')r'^2 {\rm d}r' \tag{6}$$

and the energy per mass of the shell,

$$E(r) = \frac{1}{2}\left(\frac{{\rm d}r}{{\rm d}t}\right)^2 - \frac{GM(r)}{r} - \frac{\Lambda c^2 r^2}{6}\cdot \tag{7}$$

In view of the recent interest in Friedmann models with non-zero cosmological constant Λ, we have added its contribution. The energy term determines whether the mass shells will eventually escape ($E(r) > 0$) or collapse to the center ($E(r) < 0$). The usual assumption that the mass shells do not overtake each other, i.e. there are no shell crossings, is followed here.

We attempt to solve the present day velocities of the mass shells, $v_r(r)$, for the spherically symmetric mass distribution, with the initial condition that at some point in the past these mass shells have all been very close together. That is, we assume the big bang to have happened at $t = 0$. This moment is acquired from the underlying Friedmann model, by calculating the age of the Universe $T_0 = T_0(H_0, \Omega_0, \Omega_\Lambda)$ for the set of cosmological parameters H_0, $\Omega_0 = \rho_0/\rho_{\rm cr}$, and $\Omega_\Lambda = \rho_\Lambda/\rho_{\rm cr}$, where $\rho_{\rm cr} = \frac{3H_0^2}{8\pi G}$, ρ_0 is the mass density, and $\rho_\Lambda = \frac{\Lambda c^2}{8\pi G}\cdot$ Then we find the value of the energy term $E(r)$ for each present day radius r_0, by demanding $r(T_0, E) = r_0$ and $r(0, E) = 0$, and integrating backwards in time. The integration is performed numerically for both r and v_r with

$$\dot{r} = \sqrt{2\left(\frac{GM(r)}{r} + \frac{\Lambda c^2 r^2}{6} + E\right)} \tag{8}$$

ensuring the conservation of energy, and

$$\dot{v}_r = -\frac{GM(r)}{r^2} + \frac{\Lambda c^2 r}{3}\cdot \tag{9}$$

This numerical approach is used because for $\Lambda \neq 0$ model a simple parameterized solution given in e.g. Olson & Silk (1979) does not apply. For $\Lambda = 0$, we checked the numerical calculations by the parameterized formulae.

For $t \to 0$, where the velocities grow considerably, the numerical methods confront some difficulties. Even with adapted stepsize algorithms we can not avoid all the problems. Using a fourth order Runge-Kutta method, we obtain inconsistent results, $\dot{r} \neq v_r$, when $t < \frac{T_0}{100}\cdot$ Fortunately our main concern is to calculate the dynamics at larger t, where the method proved to be robust. A comparison to the parameterized TB solution showed that the problems at small t did not have any effect on our resulting values of $E(r)$. With the $E(r)$ thus obtained, the present day velocities $v_r(r_0)|_{E=E(r_0)}$ can be calculated.

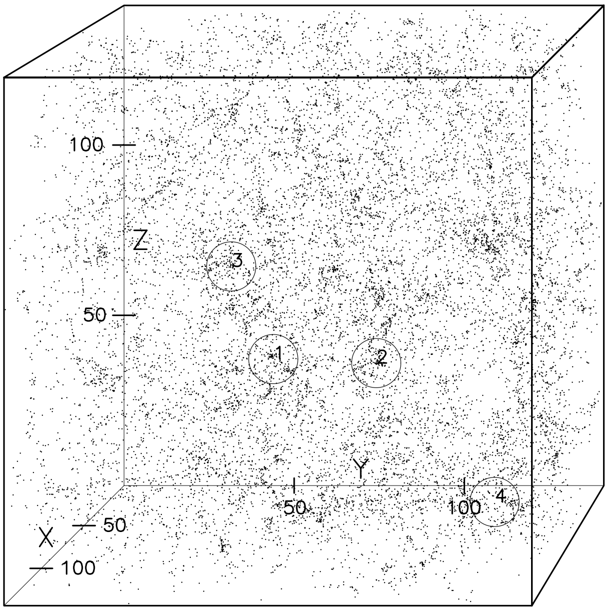

Fig. 5. The (141 h^{-1} Mpc)^3 cube of GIF N-body simulation galaxies. The simulation started with 256^3 dark halos, producing the 15 000 galaxies seen in this figure. The four circles indicate the clusters for which we studied the applicability of the TB calculations.

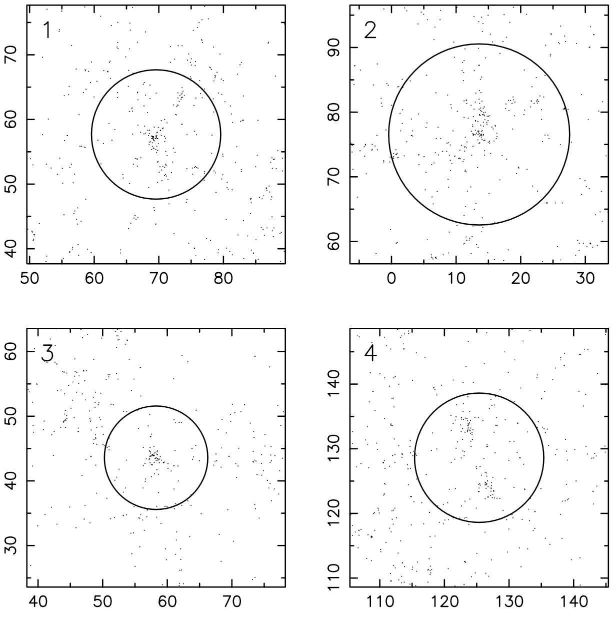

Fig. 6. The four GIF galaxy clusters extracted for further study. Figures show XY-planes from the previous figure, centered to the cluster centers. The width in Z direction of each plot is 30 Mpc. Circles with radii R_s are drawn. It is notable that these complexes are not spherically symmetric, resembling the situation with PP.

4.2. Testing the method on an N-body simulation

The TB model is a rough approximation of the dynamics of galaxy clustering. The reader may suspect that the assumption of spherical matter distribution around a galaxy cluster is perilous. In reality galaxies seem to accumulate into filamentary and wall-like structures. However, an averaged galaxy density field may be well described with a spherical model; the IRAS map, using a 12 h^{-1} Mpc smoothing, shows a roughly spherical density field around PP (Sect. 4.3). And the distribution of dark matter may be even more spherical.

How about the peculiar velocities? The many-body gravitational interplay determining the dynamics of galaxy clustering is a complicated issue, can it really be described by smooth radial TB velocities? That may seem doubtful, but, again, we rely on the power of averaging. The TB results are compared only to the average radial velocities around the center of mass.

The correspondence between the TB solutions and the averaged observational quantities is here studied with a cosmological N-body simulation. In a simulated galaxy cluster we have the advantage of knowing the true distribution of matter and the true velocities, not distorted by selection effects or observational uncertainties. And even better, we can study the evolution of the cluster and compare the matter and velocity distribution of the galaxies to those predicted by the TB model at different epochs.

In what follows we use the N-body simulation data provided by the GIF group, a German-Israeli collaboration working with the Virgo consortium project (`http://star-www.dur.ac.uk/~frazerp/virgo/`). The GIF team investigates the clustering of galaxies in a hierarchical universe (Kauffmann et al. 1999a, 1999b; Diaferio et al. 1999). They simulate structure formation in a periodical (141 h^{-1} Mpc)^3 cube using a cold dark matter, flat curvature, non-zero cosmological constant model with $\Omega_0 = 0.3$, $\Omega_\Lambda = 0.7$, and $h = 0.7$. The simulation starts with 256^3 dark matter halos with masses $1.4\ h^{-1}\ 10^{10}\ M_\odot$. The galaxies are formed at concentrations of halos, and the effects of gas cooling, star formation, and supernova feedback are taken into account. The data files at `http://www.mpa-garching.mpg.de/Virgo/data_download.html` have the positions, velocities, and luminosities of galaxies and distribution and masses of halos at six redshifts, $z = 0.00$, 0.20, 0.42, 0.62, 0.82, and 1.05, corresponding to epochs $t/T_0 = 1.00$, 0.97, 0.79, 0.67, 0.57, and 0.49. There are two sets of files, one for the galaxies (luminous matter) and one for the halos (luminous + dark matter).

Figure 5 shows the galaxies in the whole (141 h^{-1} Mpc)^3 cube at $z = 0$. We study the evolution of four large clusters in the simulation. These clusters are circled in Fig. 5 and shown individually in Fig. 6. For each of these clusters we approximate the central radius R_s by eye, and calculate the masses and the radially averaged $\delta(r)$, see Table 3. These values are similar to what we observe in the PP supercluster.

The overdensities are calculated from the halo number distribution, with a 3 h^{-1} Mpc smoothing. At this smoothing length the matter distribution in the simulation is unbiased according to Kauffmann et al. (1999a). Then we determine the center of mass and calculate the radially averaged $\delta(r)$ around each of the four clusters. For the TB calculations we use either this observed $\delta(r)$ (at $z = 0$) or

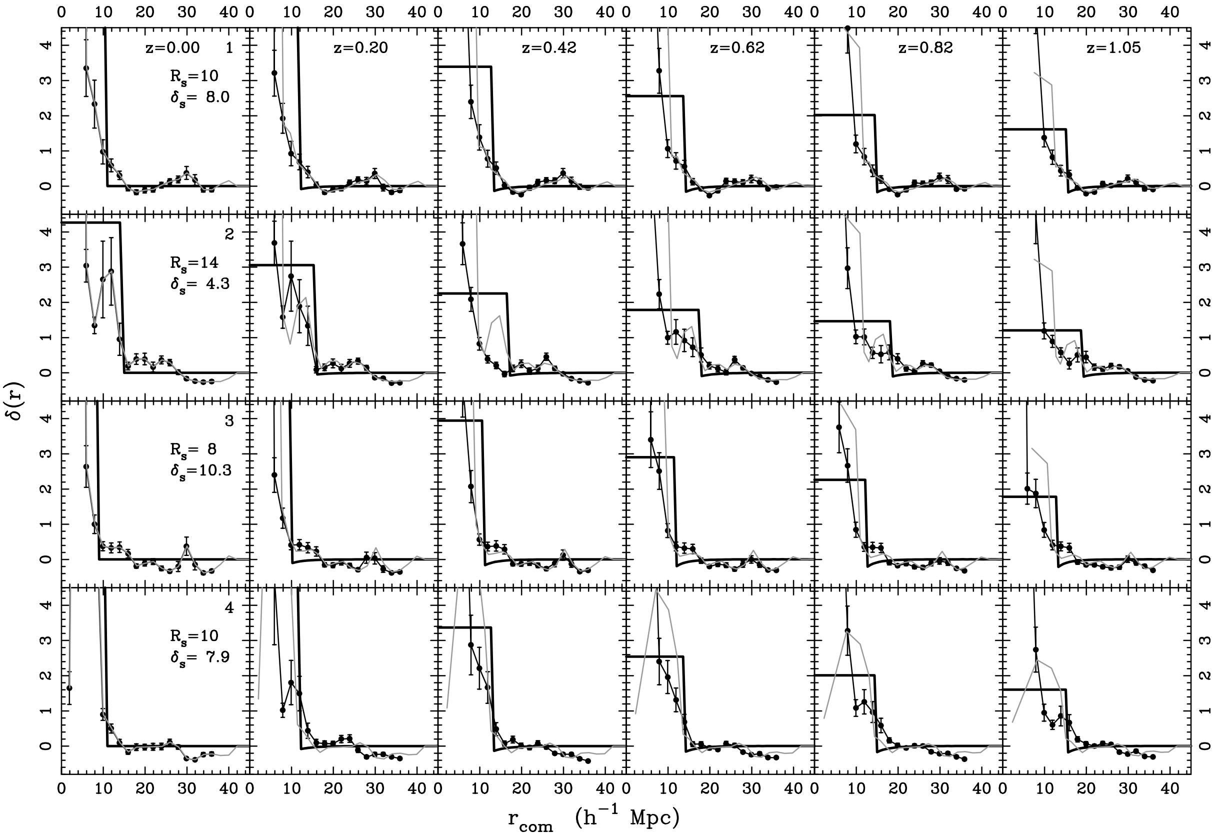

Fig. 7. The density fields $\delta(r)$ around the four simulated clusters at the six epochs between the present and $z = 1.05$. Points show the averaged $\delta(r)$ of the simulation, calculated using a 3 h^{-1} Mpc smoothing. Error bars are the $1\,\sigma$ standard deviations. Gray line is the observed density field at $z = 0$ evolved backwards in time via the TB model. Thick black line is the TB evolved "step function" toy model. R_s are the adopted cluster radii and δ_s are the average overdensities within these radii at $z = 0$.

Table 3. Radii R_s, and masses and average overdensities inside R_s, of the four simulated clusters in Fig. 6. The units are $[R_\mathrm{s}] = h^{-1}$ Mpc, $[M] = h^{-1}\,10^{15} M_\odot$.

	R_s	M	$\langle\delta\rangle_{R_\mathrm{s}}$
1	10	4.5	8.0
2	14	7.2	4.3
3	8	3.0	10.3
4	10	4.4	7.9

a "step function" toy model where $\delta(r < R_\mathrm{s}) = \langle\delta\rangle_{R_\mathrm{s}}$, and $\delta(r \geq R_\mathrm{s}) = 0$. Figure 7 shows the evolution of $\delta(r)$ in the simulation and by means of the TB model. The toy model is very instructive in showing how the density enhancements grow in amplitude and converge in comoving radius with time.

As expected, in the simulation the structures form at $z > 1$ and there is not much evolution in $\delta(r)$ from $z = 1.05$ to $z = 0$. Contrarily, in the TB evolved clusters the overdensities are low at $z = 1.05$ but grow quite steadily to the present day values. At larger r the $\delta(r)$ given by TB model follow the corresponding values of the simulation quite well at each epoch.

Figure 8 shows the comparison of the observed averaged peculiar velocities in the simulated clusters to the TB results. A similar time dependent factor as in the evolution of the density field is seen here. At earlier epochs the peculiar velocities given by the TB model are somewhat smaller than the $v_r(r)$ in the simulation. At $z = 0$ the TB values are higher, although the differences are not at a significant level.

Our conclusion is that concerning the evolution of density and velocity fields around clusters there is a marginal difference between the simulations and the TB calculations. The overdensities $\delta(r)$ are quite well approximated at large r at each epoch, and the present day peculiar velocities $v_r(r)$ are sufficiently well derived, that is, with $<1\,\sigma$ deviation, using the observed present day $\delta(r)$.

4.3. TB method applied to Perseus-Pisces

Now, how to use TB method for Perseus-Pisces where the distribution of luminuous matter apparently is not spherically symmetric? Certain restrictions and assumptions must be applied. Firstly, we isolate a sphere containing the main part of the mass, as was done in Sect. 3. Then we assume that any substructures or dynamical features inside the sphere do not affect a galaxy outside it; the sphere can effectively be replaced by a point mass located at the center. Outside the sphere, we assume the density to decrease to the average density of the universe following

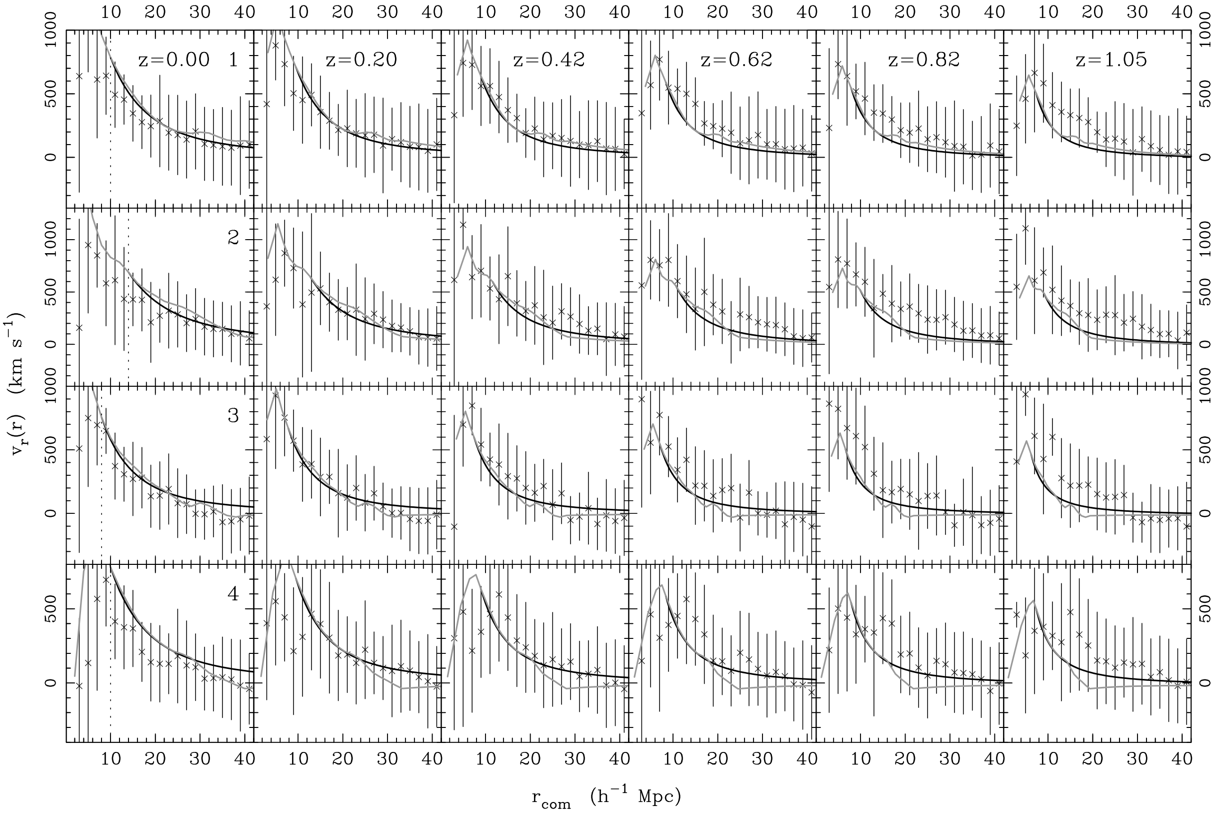

Fig. 8. The evolution of the velocities $v_r(r)$ around the four clusters. Crosses and error bars are the averaged $v_r(r)$ and their standard deviations observed in the simulation. Gray lines correspond to the observed density distribution and black lines to the toy model density distributions, evolved within the TB models.

spherical symmetry:

$$\delta(r,\theta,\phi) = \delta(r) \text{ if } r > R_\mathrm{s}$$
$$\delta(r) \to 0 \text{ for } r \gg R_\mathrm{s}$$

(R_s = radius of the sphere). After these assumptions we can apply TB equations for galaxies close to, but not inside the sphere.

The assumptions may seem doubtful. Is it not oversimplified to approximate the filamentary structure seen in the PP region with a spherical model? The filaments must produce observable non-radial motions. The main justification for our method lies in the power of averaging. Small scale non-radial peculiar velocities are smoothed away in a similar manner as a smoothed density map blurs away small scale substructure. Compare the smoothed IRAS map by Sigad et al. (1998) to the galaxy map in Fig. 2. The IRAS map shows a spherical density distribution centered in the PP, quite unlike the first glance on the individual galaxy distribution suggests. N-body simulations indicate (Sect. 4.2) that the same thing happens for the velocity fields, justifying the usage of the TB models. In any case, over 90 percent of the matter is dark and may be more symmetrically distributed. The final criterion is how well the model describes the infall pattern and predicts the total mass.

For the density distribution outside the R_s-sphere we consider three models: two toy models, a step function

$$\delta_1(r) = \begin{cases} \delta_\mathrm{PP} & \text{if } r < R_\mathrm{s}, \\ 0 & \text{if } r \geq R_\mathrm{s}, \end{cases} \tag{10}$$

a declining profile

$$\delta_2(r) = Ar^{-2}, \tag{11}$$

where A is chosen so that $M(R_\mathrm{s}) = M_\mathrm{PP}$, and a rough approximation of the smoothed density field of IRAS galaxies around PP, taken from Sigad et al. (1998), where the middle panel of their Fig. 6 shows the supergalactic plane with LG in the center and PP at $(X,Y) \approx (50, -10)$ h^{-1} Mpc. It is notable that this is a very rough approximation of the true matter distribution – the IRAS map in Sigad et al. is heavily smoothed (12 h^{-1} Mpc Gaussian filter), and the density profile $\delta_\mathrm{IRAS}(r)$ that we use is measured by eye from their figure. However, it serves well for the accuracy that we aim for with the Tolman-Bondi method. The density models and corresponding cumulative masses are shown in Fig. 9.

Figure 10 shows schematically the system under study. A galaxy is located at distance d from us. The lines of sight towards PP and the galaxy form an angle θ. The distance from PP to the galaxy is then

$$r = \sqrt{R_\mathrm{PP}^2 + d^2 - 2R_\mathrm{PP}d\cos\theta}. \tag{12}$$

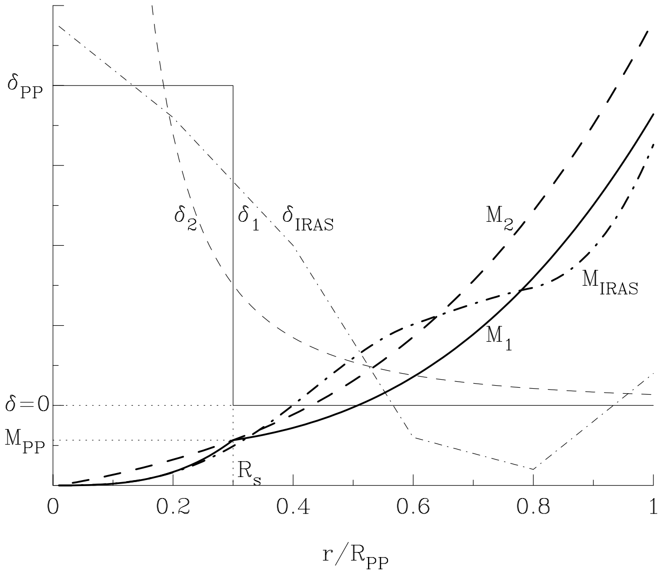

Fig. 9. Assumed spherically symmetric density distributions $\delta_1(r)$, $\delta_2(r)$ and $\delta_{\rm IRAS}(r)$, and the corresponding masses inside radius r from the PP center. Overdensity $\delta_1(r)$ and mass $M_1(r)$ are plotted with continuous, $\delta_2(r)$ and $M_2(r)$ with dashed, and $\delta_{\rm IRAS}(r)$ and $M_{\rm IRAS}(r)$ with dashed-dotted lines. See text for details.

The observable (radial) component of the peculiar velocity, $v_{d,{\rm obs}}$ (Eq. 1), of the galaxy is connected to the PP velocity field $v_r(r)$ by

$$v_{d,{\rm obs}} = -v_r(R_{\rm PP})\cos\theta \pm v_r(r)\sqrt{1-\frac{R_{\rm PP}^2\sin^2\theta}{r^2}}, \qquad (13)$$

where + is used for $d < R_{\rm PP}\cos\theta$ and − for $d > R_{\rm PP}\cos\theta$. If we have a priori knowledge of the LG infall towards PP, $v_{\rm inf} \equiv v_r(R_{\rm PP})$ we can solve PP peculiar velocities from observable quantities:

$$v_r(r) = \pm\frac{v_{d,{\rm obs}} + v_{\rm inf}\cos\theta}{\sqrt{1-R_{\rm PP}^2\sin^2\theta\,/\,r^2}}\cdot \qquad (14)$$

This is the equation used for a comparison of the TB models, giving the left hand side, and KLUN data, providing the right hand side of the equation.

5. Comparison of Tolman-Bondi and KLUN sample peculiar velocities

5.1. KLUN-PP sample

Peculiar velocities v_r of the KLUN galaxies are obtained in the following manner:

- galaxies are binned into V intervals and distances d of the bins are calculated;
- each individual galaxy is given the distance of its bin;
- distances from the PP, r, and peculiar velocities, v_r, are determined for each galaxy;
- galaxies are binned into r intervals and velocities v_r of each bin are calculated.

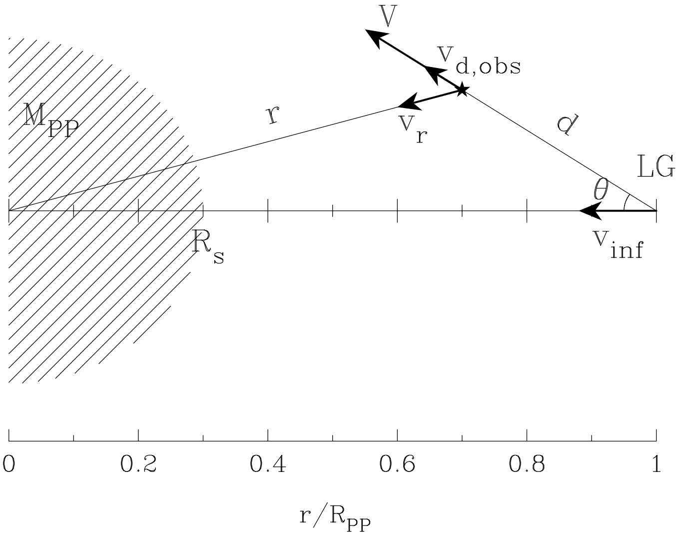

Fig. 10. Galaxy distances from the PP and LG, and observed and PP rest frame velocities are plotted in this schematic picture. Distances are normalized to the PP distance; $R_{\rm PP} = 1$, $R_{\rm s} \approx 0.3$.

First we extract a subsample (KLUN-PP) of KLUN galaxies having angular distances from the PP center less than 40° (Fig. 11). For these galaxies we calculate distances d using the NDM and the mean surface brightness dependent diameter TF relation (Sect. 2.2). Strictly speaking, the bias correction procedure provides us with an unbiased average distance at a given $d_{\rm n}$ or, as it can be shown, at a fixed kinematical distance $d_{\rm kin}$ or corrected radial velocity. Thus we bin the galaxies into velocity intervals of $\Delta V = 500$ km s^{-1}, and assign each galaxy the distance of its bin.

To avoid any difficulties in combining possibly incompatible individual distance measurements we do not use ordinary weighted averages in the bin distance determinations. The distances are deduced with more sophisticated Bayesian methods (Press 1997): probability distributions of "good" and "bad" measurements are calculated as

$$P_{\rm g,i} = \frac{1}{\sqrt{2\pi}\sigma_{\log d,{\rm i}}}\exp\left(-\frac{(\log d_{\rm i} - \log d'_{\rm B})^2}{2\sigma^2_{\log d,{\rm i}}}\right) \qquad (15)$$

and

$$P_{\rm b,i} = \frac{1}{\sqrt{2\pi}S}\exp\left(-\frac{(\log d_{\rm i} - \log d'_{\rm B})^2}{2S^2}\right) \qquad (16)$$

where $d'_{\rm B}$ is the (trial) bin distance, and $d_{\rm i}$ are the individual galaxy TF distances with errors $\sigma_{\log d,{\rm i}}$. These individual errors are calculated by

$$\sigma_{\log d,{\rm i}} = \sqrt{\sigma^2_{\rm TF} + \sigma^2_{\log D_{25},{\rm i}}} \qquad (17)$$

where $\sigma_{\rm TF} = 0.125$ (Theureau 1998) is the TF relation scatter, and $\sigma_{\log D_{25},{\rm i}}$ are the individual (log) apparent diameter measurement errors. In Eq. (16) S characterizes the standard deviation of "wrong" measurements. In practice S is assigned a large enough value, exceeding the

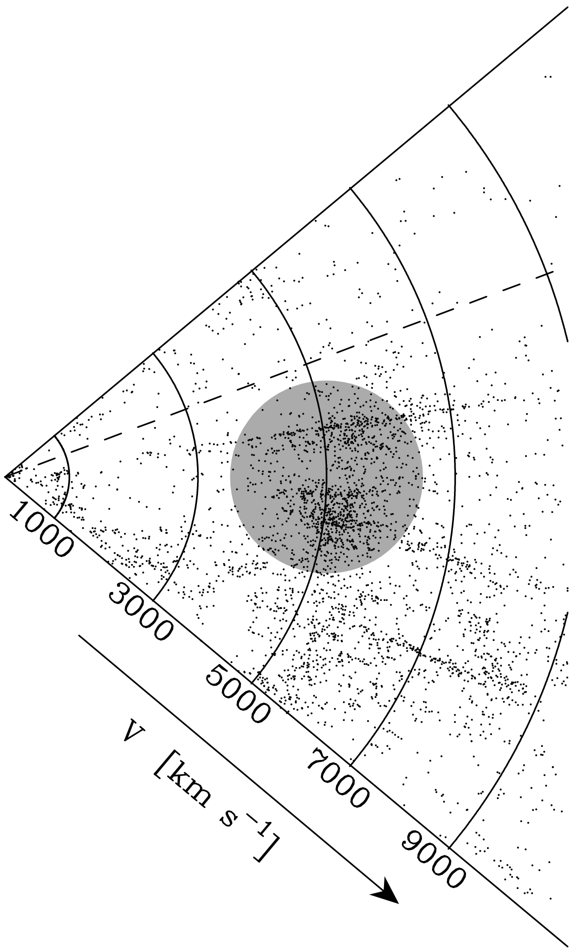

Fig. 11. LEDA galaxies within angular distance of 40° from the PP center. LG is at the apex of the cone, the gray sphere indicates the central PP region. The figure does not give a truthful representation of the galaxy distribution: distances based on redshift velocities are distorted, selection effects are strong in larger distances and projection effects in the regions close to the cone axis. The figure is a projection perpendicular to the Galactic plane, which is marked with a dashed line.

range where the measurement error would go unnoticed. We use here $S = 0.2$ (in units of $\log d$).

The probability that the binned set of data ($\mathcal{D}$) have a distance $d'_{\rm B}$ is given by

$$P(\log d'_{\rm B}|\mathcal{D}) \propto \int_p \prod_{\rm i} [pP_{\rm g,i} + (1-p)P_{\rm b,i}]\,{\rm d}p \qquad (18)$$

following Eq. (16) in Press (1997). Here p is the probability that individual distance is calculated correctly (and thus $1 - p$ is the probability for a wrong distance determination). We sum over all combinations of individual distance determinations being carried out correctly/incorrectly *and* over all values of p. Assuming uniform prior probability distributions for p and $\log d'_{\rm B}$, the sum reduces to Eq. (18). The proportionality in Eq. (18) hides the constant needed for $\sum_{\log d'_{\rm B}} P(\log d'_{\rm B}|\mathcal{D}) = 1$.

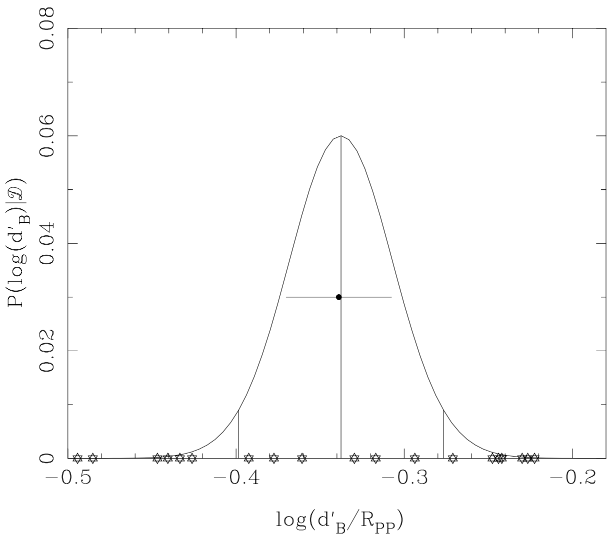

Fig. 12. An example of using the $P(\log d'_{\rm B}|\mathcal{D})$ vs. $d'_{\rm B}$ curve in the bin distance determination. Individual galaxies are plotted on the $d'_{\rm B}$ axis. Vertical lines show the adopted $d_{\rm B}$ and the 95% confidence levels. For comparison, the simple weighted mean bin distance is also drawn with $2\,\sigma$ error bars. KLUN-PP galaxies with 2500 km s^{-1} < V < 3000 km s^{-1} are shown in this example.

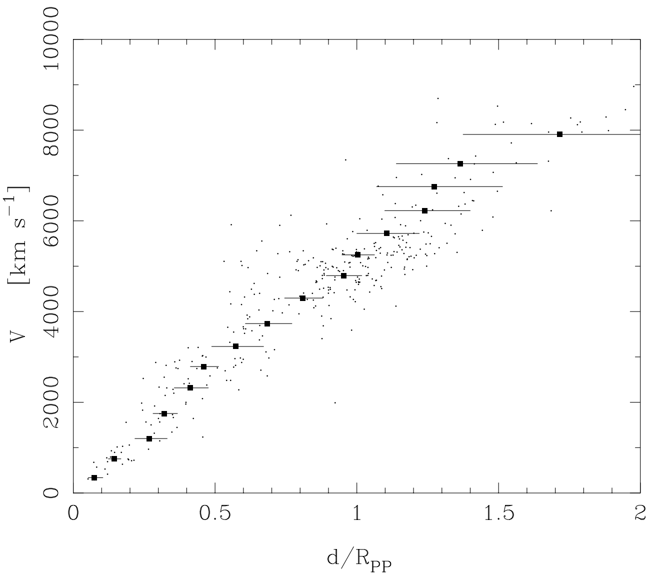

Fig. 13. KLUN-PP galaxies, bin distances and 95% error bars in a V vs. d diagram.

Actual bin distance $d_{\rm B}$ is adopted from the peak of the $P(\log d'_{\rm B}|\mathcal{D})$ vs. $\log d'_{\rm B}$ curve, and 95% confidence levels are deduced from calculating the area below the curve (Fig. 12). Figure 13 shows the individual and binned values for all the data points in the KLUN-PP sample. For comparison the binned distances are calculated also using the simple weighted mean, see Fig. 12. There are no significant differences to the values obtained with the bayesian method, the two methods deviate $<1\,\sigma$ for each $d_{\rm B}$.

The peculiar velocity field around PP is determined similarly. Firstly each galaxy is assigned its bin distance

(d_B) and 95% limit errors (denoted by σ_B). PP distances (r_i) are calculated by Eq. (12), and errors by

$$\sigma_{r,i} = \max\left(|r_i - r(d_B + \sigma_B)|, |r_i - r(d_B - \sigma_B)|\right) \qquad (19)$$

where $r(x)$ is the function of d given by Eq. (12). Thus Eq. (19) gives a safe estimate for the maximal error in the 95% confidence interval, unless the galaxy has

$$d_B - \sigma_B < R_{PP} \cos\theta < d_B + \sigma_B. \qquad (20)$$

The point at $d = R_{PP}\cos\theta$ has the lines of sight towards us and PP exactly perpendicular. There $|r_i - r(d)|$ has a local maximum. At this point the peculiar velocity towards PP is also hard to estimate (σ_v goes to infinity!). Thus we reject all galaxies restricted by Eq. (20).

Peculiar velocities are obtained with Eq. (14) and errors by

$$\sigma_{v,i} = \max\left\{|v_i - v_r(x)|; x \in (d_B - \sigma_B, d_B + \sigma_B)\right\} \qquad (21)$$

giving again a safe 95% confidence level estimate. In the end there are 220 galaxies with PP-distances and peculiar velocities from 354 galaxies in KLUN-PP before the restriction of Eq. (20). From these, 180 have $r > R_s$. Thus roughly half of the original data are lost due to the constraints.

Galaxies are then binned into PP distance intervals of $\Delta r = 0.05\,R_{PP}$. For each bin we calculate PP distances and peculiar velocities with 95% confidence levels using the Bayesian methods stated above. Notice that for the peculiar velocity calculations we need to assume a value for our infall velocity towards PP. That is, we have $v_{\rm inf} \equiv v_r(R_{PP})$ in Eq. (14), as a free parameter.

5.2. KLUN-PP vs. TB

We study how well our TB models produce the velocity field of the KLUN galaxies when the models are varied by

- Ω_0, for which we consider values 0.1, 0.2, 0.4, or 1. Majority of recent studies agrees with this range of values (Primack 2000);
- a choice of either a flat $\Lambda \neq 0$ (i.e. $\Omega_\Lambda = 1 - \Omega_0$) or an open $\Lambda = 0$ universe;
- a choice of density distribution around PP, assumed to be one of the toy models, δ_1 or δ_2 (Eqs. (10)–(11)), or the spherically symmetric approximation of the IRAS density map, $\delta_{\rm IRAS}$;
- mass of the central part of PP, for which we assign values between 2–15 $h^{-1}\,10^{15}\,M_\odot$. In the case of $\delta_{\rm IRAS}$ the mass is varied by a linear bias factor.

KLUN-PP data are adjusted by

- LG peculiar velocity towards PP, $v_{\rm inf}$ (Eq. (14)), for which we give values between 0 and 600 km s^{-1}. These limits were chosen because 0 km s^{-1} is a natural lower limit for a TB application, and after all we expect a large mass concentration such as the PP supercluster to have at least some influence on the LG. In the other end, velocities exceeding 600 km s^{-1} would have already been noticed in our motion with respect to the CMB, and are therefore not studied.

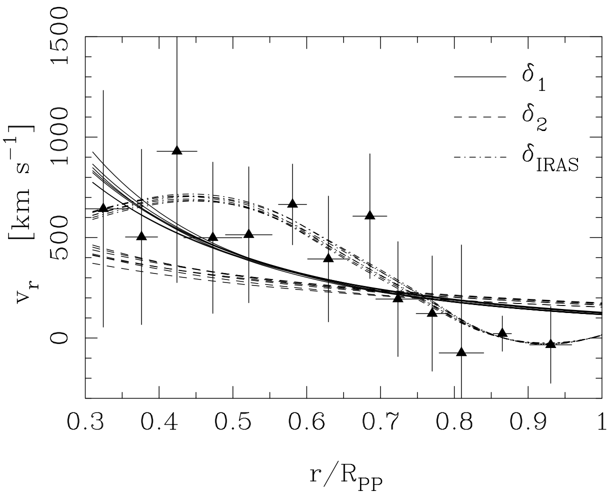

Fig. 14. Binned KLUN-PP data points and TB $v_r(r)$ curves. KLUN points are fixed with $v_{\rm inf} = 0$. The error bars are $2\,\sigma$ confidence intervals. TB curves are calculated for the three density models, δ_1, δ_2, and $\delta_{\rm IRAS}$. For each density, there is a set of curves, corresponding to the seven different cosmological models, $(\Omega_0, \Omega_\Lambda)$ = (0.1,0.9), (0.1,0.0), (0.2,0.8), (0.2,0.0), (0.4,0.6), (0.4,0.0), and (1.0,0.0).

Figure 14 shows the comparison of the peculiar velocities observed for KLUN-PP data and those predicted by the TB models. Binned KLUN-PP data points with 95% confidence level error bars are plotted in the case of $v_{\rm inf} = 0$. The curves are best fit TB curves to KLUN points, obtained by varying M_{PP} in the TB calculations. Two things are immediately obvious from looking at Fig. 14: firstly, the IRAS density model fits much better to the observations than the toy models Secondly, different cosmological models give very similar best fit curves.

To put this into numbers, we describe the goodness of fit by

$$\chi^2 = \sum_{i=1}^{N} \left(\frac{v_i - \hat{v}_i}{\sigma_i}\right)^2$$

where v_i is a KLUN data point, σ_i its $1\,\sigma$ deviation, approximated to be half of the 95% error bar, and $\hat{v}_i$ is a point from a TB curve, at the same r as the KLUN point. We get $\chi^2 = 8.67 \pm 0.20$, 12.56 ± 0.37, and 2.01 ± 0.11, and significance levels $P = 0.796 \pm 0.015$, 0.482 ± 0.029, and 0.99976 ± 0.00007 for δ_1, δ_2, and $\delta_{\rm IRAS}$, respectively. The limits reflect the variance between different cosmologies.

Figure 15 shows the formal $1\,\sigma$ confidence regions for the values of $v_{\rm inf}$ and M_{PP} obtained from fitting the $\delta_{\rm IRAS}$ TB curves to the KLUN data points. The confidence regions are defined in the following manner: the value of χ^2 is calculated for each pair of parameters ($v_{\rm inf}$, M_{PP}). Then a point in the (v, M) space belongs to the confidence region if $\chi^2(v, M) < \chi^2_{\rm min} + \tilde{\sigma}_v$, where $\chi^2_{\rm min}$ is the minimum value of χ^2 in the whole region of v = 0–600 km s^{-1} and

Table 4. The best fit values and the formal $1\,\sigma$ confidence regions of $M_{\rm PP}$ and $b_{\rm IRAS}$. See text for details. The values of $M_{\rm PP}$ are given in units of $h^{-1}\,10^{15}\,M_{\odot}$.

Ω_0	Ω_Λ	$M_{\rm PP}$	$b_{\rm IRAS}$
0.1	0.9	$2.7^{+1.4}_{-0.6}$	$0.47^{+0.08}_{-0.14}$
0.1	0.0	$3.1^{+1.4}_{-1.0}$	$0.41^{+0.14}_{-0.11}$
0.2	0.8	$3.9^{+1.8}_{-1.4}$	$0.49^{+0.24}_{-0.15}$
0.2	0.0	$3.9^{+1.8}_{-1.4}$	$0.49^{+0.24}_{-0.15}$
0.4	0.6	$5.5^{+2.2}_{-1.4}$	$0.53^{+0.20}_{-0.16}$
0.4	0.0	$5.5^{+2.2}_{-1.4}$	$0.53^{+0.20}_{-0.16}$
1.0	0.0	$9.4^{+2.9}_{-1.8}$	$0.55^{+0.20}_{-0.17}$

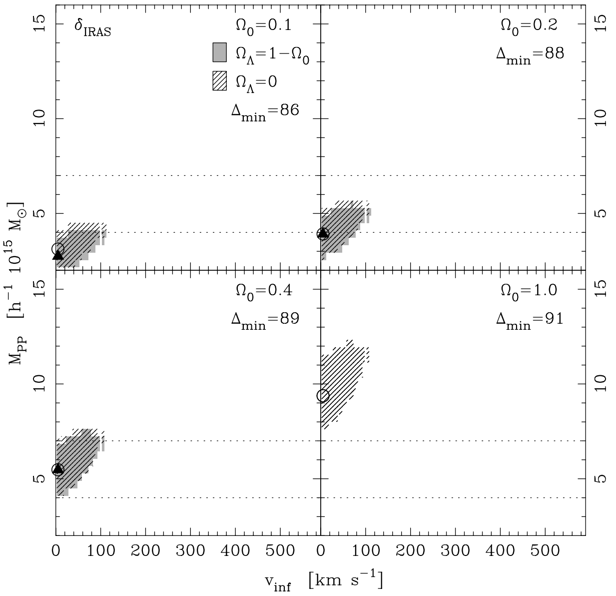

Fig. 15. The formal $1\,\sigma$ confidence regions (see text) for $v_{\rm inf}$ and $M_{\rm PP}$. The best fit values are marked with triangles for $\Omega_\Lambda = 1 - \Omega_0$ and circles for $\Omega_\Lambda = 0$. The dotted lines show the $M_{\rm PP}$ limits obtained in Sect. 3.

$M = 2$–$15\,h^{-1}\,10^{15} M_{\odot}$, and $\tilde{\sigma}_{\rm v}$ is the average of the $1\,\sigma$ errors of the binned KLUN velocities. This definition thus gives all the points in ($v_{\rm inf}$, $M_{\rm PP}$) giving $\chi^2 \approx \chi^2_{\rm min}$ within observational errors.

The confidence regions in Fig. 15 suggest that the LG infall towards PP is less than about 100 km s^{-1}. In each case the best fit, plotted in the figure as a black triangle for $\Omega_\Lambda = 1 - \Omega_0$ and a white circle for $\Omega_\Lambda = 0$, is obtained with $v_{\rm inf} = 0$. The best fit values of $M_{\rm PP}$ are coupled to the value of Ω_0; the correspondence with the range $M_{\rm PP} = 4$–$7\,h^{-1}\,10^{15}\,M_{\odot}$, which was obtained in Sect. 3, is better for $\Omega_0 = 0.2$–0.4 than for $\Omega_0 = 0.1$ or 1.

As mentioned above, the mass $M_{\rm PP}$ is varied by adjusting a bias parameter for the δ-values given by Sigad et al. (1998). Let $\delta_{\rm S}$ be the overdensity at different distances around the PP center, obtained using the contour plot in Fig. 6 of Sigad et al. (1998). Since Sigad et al. use $\Omega_0 = 1$ in their figure, $\delta_{\rm S}(r)$ must be multiplied by $\Omega_0^{-0.6}$ for a general case of $\Omega_0 \neq 1$. Then we assume a bias of the form $\Omega_0^{-0.6}\delta_{\rm S} = b_{\rm IRAS}\,\delta_{\rm IRAS}$, where $\delta_{\rm IRAS}$ gives the density which we use in the TB calculations. Increasing $b_{\rm IRAS}$ would mean decreasing the value of $M_{\rm PP}$, for example when $\Omega_0 = 0.4$, $M_{\rm PP} = 4\,h^{-1}\,10^{15}\,M_{\odot}$ requires $b_{\rm IRAS} = 0.83$ and $M_{\rm PP} = 7\,h^{-1}\,10^{15}\,M_{\odot}$ means $b_{\rm IRAS} = 0.42$. The best fit values for $M_{\rm PP}$ and $b_{\rm IRAS}$, and their formal $1\,\sigma$ confidence regions, derived from the regions in Fig. 15, are listed in Table 4.

Our conclusion from comparing the KLUN-PP peculiar velocity data to the TB-modeled velocity field is that we get a good correspondence between the two when

- the density field around PP is approximated from the IRAS galaxies, as presented by Sigad et al. (1998), with addition of a linear bias $b_{\rm IRAS} \approx 0.5$;
- the infall velocity of the LG towards the center of PP, $v_{\rm inf}$, is less than 100 km s^{-1}.

We also note that

- varying the value of Ω_0 between 0.1 and 1 and fixing $\Omega_\Lambda = 1 - \Omega_0$ or 0 have no significant effect on the results, except that;
- the mass of the central part of the PP agrees with the limits obtained with the virial theorem if $\Omega_0 = 0.2$–0.4.

5.3. Iterative corrections, p-class analysis

The first results can be used to correct the observed velocities in our NDM distance determination. With the best fit $\delta_{\rm IRAS}$ TB model shown in Fig. 14 we calculate peculiar velocities at different distances r, which are used to correct the input kinematical distance scale. The whole process of binning and solving for PP distances and peculiar velocities is then repeated with these new kinematical distances as a reference scale.

A big disadvantage in this iterative procedure is that at each iteration we lose about half of our data points due to the constraints of Eq. (20) and $r > R_{\rm s} = 0.3\,R_{\rm PP}$. Figure 16 shows how we have only 6 binned data points containing 90 individual galaxies after the first iteration. Our conclusion is that the iterative process does not in this case improve the results.

Ekholm & Teerikorpi (1994) used in their study of the peculiar velocities in the Great Attractor region a so-called p-class analysis. There the possibility of the $\log d_{\rm TF}$ not being normally distributed is taken into account by taking only the galaxies lying in the unbiased plateau of the $\langle \log H_0 \rangle (d)$ diagram. Applying the same procedure here did not give disagreeing results with the velocity patterns shown e.g. in Fig. 14, but, again, the number of points given by the p-class analysis was small.

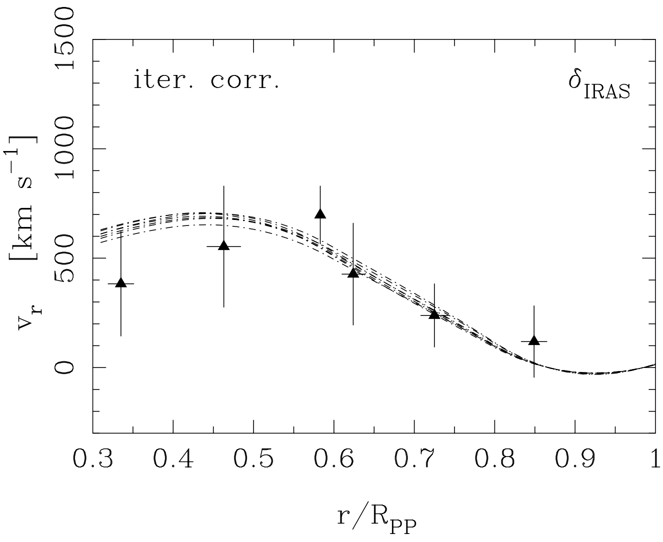

Fig. 16. Binned data points in v_r vs. r diagram after the iterative process for correcting distance determinations. Each time the PP distances are calculated, approximately half of the data are lost due to restrictions (Eq. (20)) and $r > 0.3\,R_{\rm PP}$. Only six binned data points are now present, rather than the 13 shown in Fig. 14. In this figure we have adjusted the KLUN points with $v_{\rm inf} = 0$, and the curves show the best fitted TB solutions using $\delta_{\rm IRAS}$. The best fit values are $M_{\rm PP} = 2.9$, 3.7, 5.5, and 9.4 $\times h^{-1}\,10^{15}\,M_\odot$, for $\Omega_0 = 0.1$, 0.2, 0.4, and 1.0, respectively, corresponding to bias values $b_{\rm IRAS} = 0.45$, 0.52, 0.53, and 0.55.

6. Summary

We have studied the velocity field around the Perseus-Pisces supercluster using the KLUN galaxy sample and Tolman-Bondi modeling. In the TB calculations we used a smoothed density field of IRAS galaxies, as given by Sigad et al. (1998). There is a good correspondence with the peculiar velocities given by the KLUN data and the TB models, if the infall velocity of the LG towards the PP center is assumed to be less than 100 km s^{-1} and if we add a bias in the Sigad et al. density field, $b_{\rm IRAS} \approx 0.5$. The resulting small infall velocity of the LG towards the PP region, $v_{\rm inf} < 100$ km s^{-1} disagrees with the $v_{\rm inf} \approx 350$ km s^{-1} of the earlier kinematical studies (see Sect. 1), but is consistent with the recent POTENT analysis (Dekel 1999).

The goodness of fit between the KLUN and TB velocities is not affected by varying the cosmological parameters Ω_0 and Ω_Λ within reasonable limits. However, requiring the mass of the central region of PP to be in the limits obtained with virial calculations, $M_{\rm PP} = 4$–$7\,h^{-1}\,10^{15}\,M_\odot$, we get constraints for the value of Ω_0. Then the intermediate values $\Omega_0 = 0.2$–0.4 are preferred to the more extreme $\Omega_0 = 0.1$ or $\Omega_0 = 1$. The value of Ω_Λ, assumed to be either $1 - \Omega_0$ or 0, does not have a significant effect on the results. In fact, the infall velocities around growing structures being little influenced by the presence of Λ is not so unexpected (Peebles 1984; Lahav et al. 1991).

Calculation of the virial masses of the most prominent clusters in the PP region resulted in cluster mass to luminosity ratios $M/L = 200 - 600\,h\,M_\odot/L_\odot$. Combining this with a luminosity density of the universe $\mathcal{L} = 10^{19.6\pm0.1}\,h$ W Hz^{-1} Mpc^{-3} (Lilly et al. 1996), and assuming that the M/L of the PP region is valid in the rest of the universe, we obtain $\Omega_0 = 0.1$–0.3. Allowing M/L to grow at larger scales would mean that this is a lower limit. The result agrees with recent estimates of Ω_0. In comparison, in the study of the Hubble flow around the Virgo cluster, Teerikorpi et al. (1992) found that the constraint $M/L =$ constant is inconsistent with $\Omega_0 < 0.2$ or $\Omega_0 > 1.4$. A smaller Ω_0 was possible if M/L in Virgo is larger than in the field, contrary to the usual bias scenario. The same is valid here.

One of our aims was to study the applicability of the TB method in a complex environment like the PP supercluster. TB solutions are for spherically symmetric mass distributions only, and looking at the galaxy distribution in Fig. 2, PP hardly can be taken as such. However, a smoothed density map, like the IRAS map by Sigad et al. (1998), has a spherical structure. Similarly, the small scale dynamics are smoothed away, when we use an averaged velocity map, where the radial parts of the peculiar velocities are averaged over a shell around the main galaxy concentration. This is shown not only in the compatibility of the TB results and the KLUN data, but also in a study of an N-body simulation. There it was confirmed that the radially averaged velocity field can be calculated by the TB method, using the observed smoothed density field. There were marginal differences between the TB solutions and the simulation when we looked at the peculiar velocities around large clusters at different epochs. However, at the present epoch these deviations are negligible. We argue that the Tolman-Bondi method can be used for a reliable deduction of a radially averaged velocity field around large galaxy concentrations.

Acknowledgements. We have made use of the Lyon-Meudon Extragalactic Database (LEDA) supplied by the LEDA team at the CRAL-Observatoire de Lyon (France). M.H.'s work has been supported by Finnish Cultural Foundation. We acknowledge the support by Academy of Finland projects "Cosmology in the local galaxy universe" and "Galaxy streams and structures in the local universe". The work was initiated while M.H. was visiting Osservatorio di Capodimonte in Naples. The staff in the observatory was very kind and warm-hearted and deserves to be mentioned here. We thank Dr. Yu. Baryshev for his advice concerning the TB model, and the referee for useful suggestions concerning various parts of the article.

References

Bahcall, N. A., Lubin, L. M., & Dorman, V. 1995, ApJ, 447, L81

Bahcall, N. A., Cen, R., Davé, R., Ostriker, J. P., & Yu, Q. 2000, ApJ, 541, 1

Bondi, H. 1947, MNRAS, 107, 410

Bottinelli, L., Gouguenheim, L., Paturel, G., & Teerikorpi, P. 1986, A&A, 156, 157

Bottinelli, L., Durand, N., Fouqué, P., et al. 1992, A&AS, 93, 173

Bottinelli, L., Durand, N., Fouqué, P., et al. 1993, A&AS, 102, 57

Bottinelli, L., Gouguenheim, L., Paturel, G., & Teerikorpi, P. 1995, A&A, 296, 64

Carlberg, R. G., Yee, H. K. C., & Ellingson, E. 1997, ApJ, 478, 462

Courteau, S., Faber, S. M., Burstein, D., & Willick, J. A. 1993, ApJ, 412, L51

da Costa, L. N., Freudling, W., Wegner, G., et al. 1996, ApJ, 468, L5

Dekel, A. 1994, ARA&A, 32, 371

Dekel, A., Eldar, A., Kolatt, T., et al. 1999, ApJ, 522, 1

di Nella, H., Paturel, G., Walsh, A., et al. 1996, A&AS, 118, 311

Diaferio, A., Kauffmann, G., Colberg, J. M., & White, S. D. M., MNRAS, 307, 552

Ekholm, T. 1996, A&A, 308, 7

Ekholm, T., & Teerikorpi, P. 1994, A&A, 284, 369

Ekholm, T., Lanoix, P., Teerikorpi, P., Paturel, G., & Fouqué, P. 1999, A&A, 351, 827

Ekholm, T., Lanoix, P., Teerikorpi, P., Fouqué, P., & Paturel, G. 2000, A&A, 355, 835

Freudling, W., da Costa, L. N., Wegner, G., et al. 1995, AJ, 110, 920

Fouqué, P., & Paturel, G. 1985, A&A, 150, 192

Han, M., & Mould, J. R. 1992, ApJ, 396, 453

Heisler, J., Tremaine, S., & Bahcall, J. 1985, ApJ, 298, 8

Hudson, M. J., Lucey, J. R., Smith, R. J., & Steel, J. 1997, MNRAS, 291, 488

Jerjen, H., & Tammann, G. 1993, A&A, 276, 1

Kauffmann, G., Colberg, J. M., Diaferio, A., & White, S. D. M. 1999a, MNRAS, 303, 188

Kauffmann, G., Colberg, J. M., Diaferio, A., & White, S. D. M. 1999a, MNRAS, 307, 529

Lahav, O., Lilje, P. B., Primack, J. R., & Rees, M. J. 1991, MNRAS, 251, 128

Lilly, S. J., Le Fèvre, O., Hammer, F., & Crampton, D. 1996, ApJ, 460, L1

Lynden-Bell, D., Faber, S. M., Burstein, D., et al. 1988, ApJ, 326, 19

Marinoni, C., Monaco, P., Giuricin, G., & Costantini, B. 1999, ApJ, 521, 50

Mould, J., Aaronson, M., & Huchra, J. 1980, ApJ, 238, 458

Olson, D. W., & Silk, J. 1979, ApJ, 233, 395

Paturel, G., Bottinelli, L., & Gouguenheim, L. 1994, A&A, 286, 768

Paturel, G., Bottinelli, L., di Nella, H., et al. 1997, A&AS, 124, 109

Peebles, P. J. E. 1976, ApJ, 205, 318

Peebles, P. J. E. 1984, ApJ, 284, 439

Press, W. H. 1997, Understanding data better with Bayesian and global statistical methods in Unsolved problems in astrophysics, ed. J., Bahcall, & J. P., Ostriker (Princeton University Press) [`astro-ph/9604126`]

Primack, J. R. 2000, Cosmic Flows 1999, ASP Conf. Ser. 201, ed. S., Courteau, M. A., Strauss, & J. A., Willick [`astro-ph/9912089`]

Sandage, A. 1994, ApJ, 430, 13

Sigad, Y., Eldar, A., Dekel, A., Strauss, M. A., & Yahil, A. 1998, ApJ, 495, 516

Small, T. A., Ma, C., Sargent, W. L. W., & Hamilton, D. 1998, ApJ, 492, 45

Strauss, M. A. 2000, Cosmic Flows 1999, ASP Conf. Ser. 201, ed. S., Courteau, M. A., Strauss, & J. A., Willick [`astro-ph/9908325`]

Teerikorpi, P. 1975, A&A, 45, 117

Teerikorpi, P. 1984, A&A, 141, 407

Teerikorpi, P. 1997, ARA&A, 35, 101

Teerikorpi, P., Bottinelli, L., Gouguenheim, L., & Paturel, G. 1992, A&A, 260, 17

Theureau, G. 1998, A&A, 331, 1

Theureau, G., Hanski, M., Ekholm, T., et al. 1997, A&A, 322, 730

Theureau, G., Rauzy, S., Bottinelli, L., & Gouguenheim, L. 1998a, A&A, 340, 21

Theureau, G., Bottinelli, L., Coudreau-Durand, N., et al. 1998b, A&AS, 130, 333

Tolman, R. C. 1934, Proc. Nat. Acad. Sci., 20, 169

Tully, R., & Fouqué, P. 1985, ApJS, 58, 67

Wegner, G., Haynes, M. P., & Giovanelli, R. 1993, AJ, 105, 1251

Willick, J. A. 1990, ApJ, 351, L5

Willick, J. A. 1991, Ph. D. Thesis, University of California, Berkeley

Yahil, A., Tammann, G., & Sandage, A. 1977, ApJ, 217, 903